Ain Shams Engineering Journal 14 (2023) 102124

Contents lists available at ScienceDirect

Ain Shams Engineering Journal

journal homepage: www.sciencedirect.com

Evaluation of bioconvection for sinusoidally moving Jeffrey nanoparticles in view of temperature dependent thermal conductivity and Cattaneo-Christov heat diffusion model

Jawaher Alzahrani [a], Samaira Aziz [b], Maha Raoof Hamoudi [c], Shayma Hamza Sadon [d], Quynh Hoang Le [e,f,*], Sami Ullah Khan [g], Iftikhar Ahmad [b]

[a] Department of Mathematics, College of Education, Majmmah University, Al-Majmaah 11952, Saudi Arabia
[b] Department of Mathematics, University of Azad Jammu & Kashmir Muzaffarabad, 13100, Pakistan
[c] Department of Natural Resources Engineering and Management, University of Kurdistan Hewler, Erbil, Iraq
[d] Department of Petroleum & Mining Engineering, The Faculty of Engineering, Tishk International University, Erbil, Kurdistan Region, Iraq
[e] Institute of Research and Development, Duy Tan University, Da Nang, Vietnam
[f] School of Medicine and Pharmacy, Duy Tan University, Da Nang, Vietnam
[g] Department of Mathematics, COMSATS University Islamabad, Sahiwal 57000, Pakistan

ARTICLE INFO

Article history:
Received 2 August 2022
Revised 2 November 2022
Accepted 12 December 2022
Available online 18 January 2023

Keywords:
Nanofluids
Bioconvection
Jeffrey fluid
Variable thermal conductivity
Cattaneo-Christov double diffusion
Bi-directional accelerated surface

ABSTRACT

With impressive thermal outcomes, the nanofluids present multidisciplinary applications in the cooling processes, thermal systems, extrusion processes, heat storage devices and many more. The aim of current research is to inspect thermal impact of Jeffrey fluid with tiny particles under the assumptions of variable thermal conductivity. The problem is supported with applications of chemical reaction, activation energy and magnetic force. For heat and mass transfer phenomenon, Cattaneo-Christov diffusion theories have been implemented. The formulated model is solved by using the homotopy analysis method (HAM) with excellent accuracy. The graphical analysis is performed with specified range of parameters like $0.2 \leqslant H \leqslant 0.8$, $0.1 \leqslant \varpi \leqslant 1.7$, $0.0 \leqslant N \leqslant 1.5$, $0.0 \leqslant \Pi \leqslant 3.1$, $0.3 \leqslant \gamma \leqslant 0.6$, $0.6 \leqslant \Psi \leqslant 3.2$, $0.5 \leqslant \Omega \leqslant 2.0$, $0.0 \leqslant \Sigma \leqslant 1.5$, $0.2 \leqslant N_t \leqslant 1.7$, $1.0 \leqslant Pr \leqslant 1.9$, $0.5 \leqslant Sc \leqslant 1.4$, $0.3 \leqslant \beta \leqslant 1.5$, $0.1 \leqslant \varepsilon \leqslant 1.0$, $0.2 \leqslant N_b \leqslant 1.7$. The assessment of flow parameters is graphically evaluated. It is observed that both velocity profiles periodically enhance for Deborah number while temperature, microorganisms and concentration distributions decelerate. The greater estimates of variable thermal conductivity and heat generation improve the temperature distribution while conflicting scenario ensures for thermic relaxation constant.

1. Introduction

In the fourth industrial revolution, miniaturization is considered to be the next-generation device in the electronic subindustry. However, effective management of thermal energy around heat-generating electronic components compacted in a constrained environment remains a challenge. In our world of smart devices, it is adduced that overheat at diminutive length-scale could translate to a significant loss in component performance, impairment of device reliability which is a precursor for system failure. More so, since the failure factor in miniaturized electronic products increases exponentially with internal temperature, thermal management is considered as the lifeline in compact-sized dependent on the electronic devices. Hence, thermal energy control with nanofluid has been considered as the veritable technology for dissipating heat in multi-cascaded electronic components. Therefore, because of the inherent excellent thermal and heat transfer properties, nanofluids have been accepted as a candidate coolant for cooling and thermal management for microelectronics. Being a nanoparticle-mediated media, nanofluid consists of particulate nanometer-sized species in colloidal suspension engineered to achieve a unique capacity of high thermal effective-

* Corresponding author.
E-mail address: qnleh@duytan.edu.vn (Q.H. Le).

Peer review under responsibility of Ain Shams University.

Production and hosting by Elsevier

https://doi.org/10.1016/j.asej.2023.102124
2090-4479/

Nomenclature

(u, v)	velocity components
$\mathbf{B}_0$	magnetic field constant strength
ω	angular frequency
T_w	temperature
C_w	nanoparticles concentration
n_w	microorganisms density
T_∞	free stream temperature
C_∞	free stream concertation
n_∞	free stream microorganisms density
v	kinematic viscosity
Ω	ratio among relaxation and retardation times
ϑ	electric conductivity
α_*	represents retardation time
g	gravitational acceleration
$\wp$	thermal expansion coefficient
$\delta_{\bar{T}}$	thermal relaxation time
σ_*	microorganisms volume
$k(T)$	thermal conductivity
$\mathcal{Q}$	heat generation volumetric rate
$\mho$	the heat capacities ratio
$\delta_{\bar{C}}$	solutal relaxation time
K	designates reaction rate
m	be the rate constant
$E_\odot$	symbolizes activation energy
$\beta_\odot$	the Boltzmann constant
$\Re$	indicates chemotaxis constant
$\Im$	be the swimming cell speed
D_T	diffusivity for thermophoresis
D_m	diffusivity for microorganisms
D_B	diffusivity for Brownian
ρ_p	nanoparticles density
ρ_m	microorganisms density
ρ_f	base fluid density
Ψ	Deborah number
H	Magnetic parameter
ϖ	mixed convection
N	buoyancy ratio parameter
Π	bioconvected Rayleigh number
Pr	Prandtl number
Ξ	heat generation constant
N_b	Brownian motion
δ_1	thermic relaxation constant
N_t	thermophoresis
S	angular frequency to stretching rate ratio
Sc	Schmidt number
δ_2	solutal relaxation
Δ	reaction rate
Y	bioconvected Lewis number
Λ	temperature difference
β	bioconvected Peclet number
Θ	activation energy
Γ	concentration difference constant for microorganisms
γ	stretching ratio
Sh_x	local Sherwood number
Nn_x	motile density number
Nu_x	local Nusselt number

ness in cooling processes. There is exhaustive literature on the usefulness of nanofluid has been presented in recent years. Reddy et al. [1] addressed the nanofluid properties to enhance thermal impact of water with chemical reactive species. Sreedevi et al. [2] reported the onset of nanoparticles against wedge flow under the applications of radiated phenomenon. The nanofluid due to swirling of cylinder via modified thermal expressions was inspected by Reddy et al. [3]. Sreedevi and Reddy [4] evaluated the nanofluid thermal efficiencies with Williamson fluid numerically. Abdelsalam et al. [5] identified the hybrid Casson nanofluid material flow via sinusoidal channel. Alsharif et al. [6] claimed the DC operated phenomenon for hybrid nanofluid following the electroosmosis phenomenon. Thumma et al. [7] expressed the nanofluid elongated by moving space under impact of additional heating source. Bhatti et al. [8] considered the solar energy application with entertaining of nanoparticles in elastic regime. Mekheimer et al. [9] rpeoted the drug delivery associated to the human blood via utilization of nanoparticles via computational approach. The dynamic of nanoparticles in viscoelastic foundation with nanoplate was inspected by Liu et al. [10]. Vinh et al. [11] observed the role of nonlocal parameters in nanoshells with porous layer. Vinh et al. [12] performed computational simulations for nanoshells under consideration of nonlocal factors. Bouafia et al. [13] used the integral plate hypothesis to discuss the nanofluids problem in elastic medium. Heidari et al. [14] depicted the thermal mechanics of nanotubes in wavy surface. Song et al. [15] examined the migration of nanofluid conveying the enhancement in water base material in heated surface. Oke et al. [16] reported the thermal transportation of nanoparticles with 47 nm diameter under heat source effects. Rajakarunakaran et al. [17] presented the selp compacting analysis with nanoparticles. Liu et al. [18] performed molecular dynamic analysis for nanoparticles with different volume fraction. Li et al. [19] suggested the applications of drug delivery with interaction of carbon nanotubes. The applications of graphene oxide nanoparticles subject to the solar collector was presented by Huhemandula et al. [20].

The phenomenon of bioconvection is characterized by flow instability in the hydrodynamic field which is mediated by a complex of stimuli-induced effects on self-propelling motile organisms resident in the fluid media. In order to effect its locomotive action in the fluid medium, microorganisms in nature portend a dual-density behavior with the upper dense surface to trigger sufficient disruption in the fluid layer which is classified as microscopic convection. The causative stimuli of bioconvective transport decide the christening of macroscopic convection in the fluid media. For instance, chemostatic is caused by chemical species while oxytactic is mediated by an abundance of oxygen, the gravitational force is seen to control the formation of gyrotactic bioconvection. The repeated instabilities in the fluid layer associated with bioconvection are believed to mediate cross-layer mixing of constituents in the fluidic media in which micro-organisms are embedded have been described as a passive strategy for improving convective thermal transport in nanofluid-dependent electronic cooling strategy. Khan and Shehzad [21] address the gyrotactic bioconvection analysis for nanofluid by using Carreau fluid model. Waqas et al. [22] expressed the Joule heating influence for microorganism flow via stretchable moving space. Azam et al. [23] intended the interreference of cross nanofluid with expression of bioconvection numerically. Hussain et al. [24] observed the stability of nanofluid in wavy surface with dynamic of microorganisms. The double diffusion layer for micropolar nanomaterial additionally incorporated with microorganisms was focused in the investigation of Habib et al. [25]. Chu et al. [26] addressed the quantitative analysis of nanofluid via stretched disk with gyrotactic microorganisms. Xia et al. [27] preformed the computational aspect of bioconvection for Eyring-Powell nanofluid with irreversibility framework. Habib et al. [28] used the slip phenomenon for examining the bioconvection association of nanofluid with role of electric force. Elbashbe-

shy et al. [29] responded the bioconvection applications in stretching cylinder with nanomaterials. According to Makinde et al. [30], bioconvection is unavoidable because numerous bacteria (organisms) are present, and it is well-known that many bacteria can be harmed and occasionally killed by high temperatures. On the other hand, the organism known as a thermophile is frequently found in the earth's warm climates. Bioconvection was defined by Animasaun et al. [31] as the movement of numerous small organisms in a fluid, particularly free-swimming zooplankton in water. In other words, it will always show itself in shallow suspensions of haphazardly moving microorganisms that, on average, swim upward and are slightly denser than water.

Although several constitutive models have been utilized to narrate rheological shear-thinning/shear-thickening behavior in non-Newtonian fluids, these constitutive relations are limited in practical cases where the requirement for extensive experimental shear rate data is paramount for design decision making processes. For instance, during rheometer studies on micromechanics of complex fluids such as gels and polymeric materials, exhaustive data on shearing effect over a wide range of thermal and loading conditions are captured in minimal exposure. The Jeffrey fluid model is the extension of viscous fluid model which captured the predict elastic and memory features associated to the dilute polymer solutions and biological liquids. Many investigations are reported by investigators by using the Jeffrey fluid model under diverse flow features [32–34].

Motivated by above presented literature survey on bioconvection flow of nanofluids, the aim of current work is to report the heat and mass transfer phenomenon in three-dimensional Jeffrey nanofluid with microorganism. The analysis is performed in view of variable thermal conductivity. The modified Cattaneo-Christov diffusion theories and generation/absorption features are also implemented to perform the heat transfer analysis. Moreover, thermal transport is augmented with the imposition of the magnetic field in a media comprising of microorganisms embedded in Jeffrey nanofluid. The source of flow is bidirectional accelerating moving surface with periodic motion [35,36]. The motivations for considering the oscillatory stretching surface are associated with different industrial and engineering phenomenon like manufacturing processes, fiber spinning, hot rolling, plastic manufacturing, food production. Moreover, the thermal transport due to moving surfaces present exclusive applications in cooling of strips, foodstuff processing, chemical processes, design of heat exchangers etc. The analytical scheme namely homotopy analysis scheme is implemented for simulations. The solution accuracy is verified. The analysis of important physical parameters is presented with sufficient emphasis on thermal dissipation and reactive transport for bio-convective nanofluid model.

2. Problem formulation

Three-dimensional bio-convective flow of Jeffrey nanomaterial towards periodically moving surface is assumed here. Periodically accelerated surface $(z = 0)$ moves with velocities $u = ax\sin\omega t$ and $v = by\sin\omega t$ along $x-$ and $y-$ directions, correspondingly, where a, b are stretching rates while ω signifies angular frequency. Here, flow is presumed at $z \geqslant 0$ and magnetic field $\mathbf{B}_0$ of constant strength is considered along $z-$ direction. Thermal and mass transportation feature are analyzed by utilizing modified diffusion laws. Heat transfer analysis is further accomplished by considering variable thermal conductivity and heat generation/absorption features. Additionally, this exploration involves the significances of activation energy with chemical reaction rate. Furthermore, the moving surface retained uniform temperature T_w, nanoparticles concentration C_w and microorganisms density n_w, whereas free stream nanofluid temperature, concentration and microorganisms density is signified by T_∞, C_∞ and n_∞, respectively (Fig. 1). All these assumptions for unsteady flow model leads to the resulting boundary layer expressions [35,36]:

$$\frac{\partial u}{\partial x}+\frac{\partial v}{\partial y}+\frac{\partial w}{\partial z}=0, \tag{1}$$

$$\begin{aligned}&\frac{\partial u}{\partial t}+u\left(\frac{\partial u}{\partial x}\right)+v\left(\frac{\partial u}{\partial y}\right)+w\left(\frac{\partial u}{\partial z}\right)=\frac{\nu}{(1+\Omega)}\left(\frac{\partial^2 u}{\partial z^2}\right)+\frac{\nu\alpha_*}{(1+\Omega)}\\&\left(\begin{array}{c}\frac{\partial^3 u}{\partial z^2\partial t}+v\frac{\partial^3 u}{\partial y\partial z^2}+w\frac{\partial^3 u}{\partial z^3}\\+u\frac{\partial^3 u}{\partial x\partial z^2}+\left(\frac{\partial v}{\partial z}\right)\left(\frac{\partial^2 u}{\partial y\partial z}\right)\\+\left(\frac{\partial u}{\partial z}\right)\left(\frac{\partial^2 u}{\partial x\partial z}\right)+\left(\frac{\partial w}{\partial z}\right)\left(\frac{\partial^2 u}{\partial z^2}\right)\end{array}\right)-\frac{\vartheta\mathbf{B}_0^2 u}{\rho_f}+\frac{g}{\rho_f}\Big[\rho_f\wp(1-C_\infty)(T-T_\infty)\\&-\left(\rho_p-\rho_f\right)(C-C_\infty)-\sigma_*(\rho_m-\rho_f)(n-n_\infty)\Big],\end{aligned} \tag{2}$$

$$\begin{aligned}&\frac{\partial v}{\partial t}+u\frac{\partial v}{\partial x}+v\frac{\partial v}{\partial y}+w\frac{\partial v}{\partial z}\\&=\frac{\nu}{(1+\Omega)}\left(\frac{\partial^2 v}{\partial z^2}\right)+\frac{\nu\alpha_*}{(1+\Omega)}\left(\begin{array}{c}\frac{\partial^3 v}{\partial z^2\partial t}+v\frac{\partial^3 v}{\partial y\partial z^2}+w\frac{\partial^3 v}{\partial z^3}\\+\left(\frac{\partial u}{\partial z}\right)\left(\frac{\partial^2 v}{\partial x\partial z}\right)+u\frac{\partial^3 v}{\partial x\partial z^2}\\+\left(\frac{\partial w}{\partial z}\right)\left(\frac{\partial^2 v}{\partial z^2}\right)+\left(\frac{\partial v}{\partial z}\right)\left(\frac{\partial^2 v}{\partial y\partial z}\right)\end{array}\right)-\frac{\vartheta\mathbf{B}_0^2 v}{\rho_f},\end{aligned} \tag{3}$$

$$\begin{aligned}&\tfrac{\partial T}{\partial t}+u\tfrac{\partial T}{\partial x}+v\tfrac{\partial T}{\partial y}+w\tfrac{\partial T}{\partial z}+\delta_T\\&\left[\begin{array}{c}2u\frac{\partial^2 T}{\partial\tilde{x}\partial t}+w^2\frac{\partial^2 T}{\partial z^2}+v^2\frac{\partial^2 T}{\partial y^2}+u^2\frac{\partial^2 T}{\partial x^2}+2w\frac{\partial^2 T}{\partial z\partial t}+w\frac{\partial u}{\partial z}\frac{\partial T}{\partial x}\\+v\left(\frac{\partial v}{\partial y}\frac{\partial T}{\partial y}+\frac{\partial w}{\partial y}\frac{\partial T}{\partial z}\right)+u\left(\frac{\partial u}{\partial x}\frac{\partial T}{\partial x}+\frac{\partial v}{\partial x}\frac{\partial T}{\partial y}+\frac{\partial w}{\partial x}\frac{\partial T}{\partial z}\right)\\+\frac{\partial u}{\partial t}\frac{\partial T}{\partial x}+\frac{\partial v}{\partial t}\frac{\partial T}{\partial y}+\frac{\partial w}{\partial t}\frac{\partial T}{\partial z}+\frac{\partial^2 T}{\partial t^2}+v\frac{\partial u}{\partial y}\frac{\partial T}{\partial x}+w\frac{\partial v}{\partial z}\frac{\partial T}{\partial y}\\+2v\left(u\frac{\partial^2 T}{\partial x\partial y}+w\frac{\partial^2 T}{\partial y\partial z}+\frac{\partial^2 T}{\partial y\partial t}\right)+w\left(2u\frac{\partial^2 T}{\partial x\partial z}+\frac{\partial w}{\partial z}\frac{\partial T}{\partial z}\right)\end{array}\right]\\&=\tfrac{1}{\rho c_p}\tfrac{\partial}{\partial z}\left(k(T)\tfrac{\partial T}{\partial z}\right)+\tfrac{Q}{(\rho c)_{\hat{f}}}(T-T_\infty)+\upsilon\left(D_B\tfrac{\partial C}{\partial z}\tfrac{\partial T}{\partial z}+\left(\tfrac{\partial T}{\partial z}\right)^2\tfrac{D_T}{T_\infty}\right),\end{aligned} \tag{4}$$

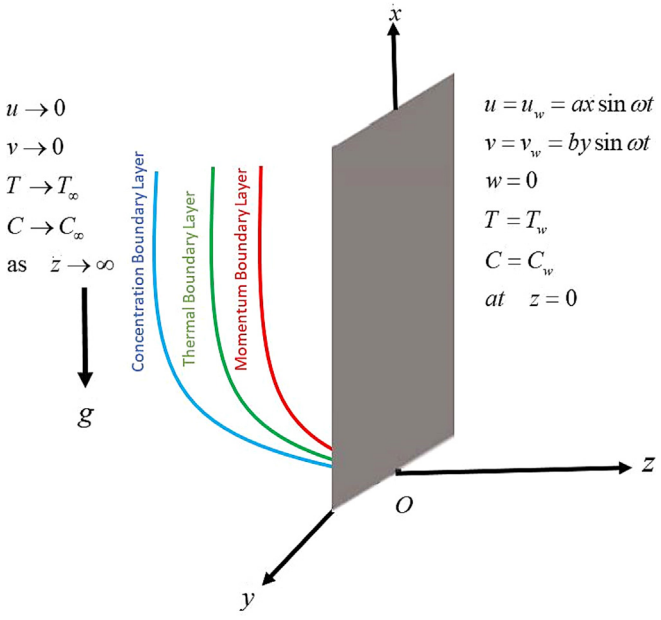

Fig. 1. Flow illustration of problem.

$$\frac{\partial C}{\partial t}+u\frac{\partial C}{\partial \tilde{x}}+v\frac{\partial C}{\partial \tilde{y}}+w\frac{\partial C}{\partial \tilde{z}}+\delta_C\left[\begin{array}{c}2u\frac{\partial^2 C}{\partial x\partial t}+w^2\frac{\partial^2 C}{\partial z^2}+v^2\frac{\partial^2 C}{\partial y^2}+u^2\frac{\partial^2 C}{\partial x^2}+2w\frac{\partial^2 C}{\partial z\partial t}+w\frac{\partial u}{\partial z}\frac{\partial C}{\partial x}\\+v\frac{\partial v}{\partial y}\frac{\partial C}{\partial y}+u\left(\frac{\partial u}{\partial x}\frac{\partial C}{\partial x}+\frac{\partial v}{\partial x}\frac{\partial C}{\partial y}+\frac{\partial w}{\partial x}\frac{\partial C}{\partial z}\right)+v\frac{\partial w}{\partial y}\frac{\partial C}{\partial z}\\+\frac{\partial u}{\partial t}\frac{\partial C}{\partial x}+\frac{\partial v}{\partial t}\frac{\partial C}{\partial y}+\frac{\partial w}{\partial t}\frac{\partial C}{\partial z}+\frac{\partial^2 C}{\partial t^2}+v\frac{\partial u}{\partial y}\frac{\partial C}{\partial x}+w\frac{\partial v}{\partial z}\frac{\partial C}{\partial y}\\+2v\left(u\frac{\partial^2 C}{\partial x\partial y}+w\frac{\partial^2 C}{\partial y\partial z}+\frac{\partial^2 C}{\partial y\partial t}\right)+w\left(2u\frac{\partial^2 C}{\partial x\partial z}+\frac{\partial w}{\partial z}\frac{\partial C}{\partial z}\right)\end{array}\right]=D_B\frac{\partial^2 C}{\partial z^2}+\left(\frac{D_T}{T_\infty}\right)\frac{\partial^2 T}{\partial z^2}-\mathrm{K}_r^2(C-C_\infty)\left(\frac{T}{T_\infty}\right)^m\exp\left(\frac{-E_\odot}{\beta_\odot T}\right). \tag{5}$$

$$\frac{\partial n}{\partial t}+u\frac{\partial n}{\partial x}+v\frac{\partial n}{\partial y}+w\frac{\partial n}{\partial z}+\frac{\Re\Im}{\left(C_w-C_\infty\right)}\left[\frac{\partial}{\partial z}\left(n\frac{\partial C}{\partial z}\right)\right]=D_m\frac{\partial^2 n}{\partial z^2}. \tag{6}$$

with suitable boundary constraints [35,36]:

$$\left.\begin{array}{l}u=ax\sin\omega t,\quad v=by\sin\omega t,\quad w=0,\quad n=n_w,\quad T=T_w,\\C=C_w,\quad at\quad z=0,\quad t>0,\quad u\to 0,\quad \frac{\partial u}{\partial z}\to 0,\quad v\to 0,\\\frac{\partial v}{\partial z}\to 0,\qquad T\to T_\infty,\qquad C\to C_\infty,\ n\to n_\infty,\quad \text{as}\quad z\to\infty.\end{array}\right\} \tag{7}$$

Here, v refers kinematic viscosity, Ω denotes ratio among relaxation and retardation times, ϑ stands for electric conductivity, α_* represents retardation time, g the gravitational acceleration, $\wp$ denotes thermal expansion coefficient, $\delta_{\tilde{T}}$ indicates thermal relaxation time, σ_* the microorganisms volume, $k(T)$ refers thermal conductivity, Q denote heat generation volumetric rate, $\mho=\frac{(\rho c)_{\tilde{n}}}{(\rho c)_{\tilde{f}}}$ the heat capacities ratio, $\delta_{\tilde{C}}$ be solutal relaxation time, K designates reaction rate, m be the rate constant, $E_\odot$ symbolizes activation energy, $\beta_\odot$ the Boltzmann constant, $\Re$ indicates chemotaxis constant, $\Im$ be the swimming cell speed, $\left(\rho_p,\rho_m,\rho_f\right)$ refers corresponding densities for nanoparticles, microorganisms and base fluid, (D_T,D_m,D_B) denotes corresponding diffusivities for thermophoresis, microorganisms and Brownian.

Furthermore, the mathematical expression used for variable $k(T)$ is:

$k(T)=k_\infty(1+\varepsilon\theta)$, where ε being small parameter, k_∞ denotes thermal conductivity at ambient zone, while θ signifies dimensionless temperature.

To obtain dimensionless expressions, the related transformations are [35,36]:

$$\left.\begin{array}{llll}u=axf_\xi(\xi,\tau), & w=-\sqrt{\nu a}[f(\xi,\tau)+g(\xi,\tau)], & v=ayg_\xi(\xi,\tau) & \tau=t\omega,\\\xi=\sqrt{\frac{a}{\nu}}z, & \phi(\xi,\tau)=\frac{C-C_\infty}{C_w-C_\infty}, & \theta(\xi,\tau)=\frac{T-T_\infty}{T_w-T_\infty}, & \chi(\xi,\tau)=\frac{n-n_\infty}{n_w-n_\infty}.\end{array}\right\} \tag{8}$$

In behalf of (8), Eqs. (1)–(7) are transmuted as:

$$f_{\xi\xi\xi}-(1+\Omega)\left(f_\xi^2+Sf_{\xi\tau}-(f+g)f_{\xi\xi}+\mathrm{H}^2\mathrm{f}_\xi\right)+\Psi\left(\begin{array}{c}\mathrm{Sf}_{\xi\xi\xi\tau}-(\mathrm{g}+\mathrm{f})\mathrm{f}_{\xi\xi\xi\xi}\\+\mathrm{f}_{\xi\xi}^2-\mathrm{g}_\xi\mathrm{f}_{\zeta\xi\xi}\end{array}\right)+(1+\Omega)(\varpi\theta-\varpi\mathrm{N}\phi-\varpi\Pi\chi)=0, \tag{9}$$

$$g_{\xi\xi\xi}-(1+\Omega)\left(g_\xi^2+Sg_{\xi\tau}-(f+g)g_{\xi\xi}+\mathrm{H}^2\mathrm{g}_\xi\right)+\Psi\left(\begin{array}{c}\mathrm{Sg}_{\xi\xi\xi\tau}-(\mathrm{g}+\mathrm{f})\mathrm{g}_{\xi\xi\xi\xi}\\+\mathrm{g}_{\xi\xi}^2-\mathrm{f}_\xi\mathrm{g}_{\xi\xi\xi}\end{array}\right)=0, \tag{10}$$

$$(1+\varepsilon\theta)\theta_{\xi\xi}+\varepsilon\theta_\xi^2+\mathrm{Pr}\left(\begin{array}{c}g\theta_\xi+f\theta_\xi-S\theta_\tau+N_t\theta_\xi^2\\+\Xi\theta+\mathrm{N_b}\theta_\xi\phi_\xi\end{array}\right)-\mathrm{Pr}\delta_1\left(\begin{array}{c}S^2\theta_{\tau\tau}-\mathrm{S}(\mathrm{f}_\tau\theta_\xi+\mathrm{g}_\tau\theta_\xi)\\-2\mathrm{S}(\mathrm{g}+\mathrm{f})\theta_{\tau\xi}+(\mathrm{g}+\mathrm{f})^2\theta_{\xi\xi}\\+(\mathrm{f}_\xi+\mathrm{g}_\xi)(\mathrm{f}+\mathrm{g})\theta_\xi\end{array}\right)=0, \tag{11}$$

$$\phi_{\xi\xi}+Sc(g\phi_\xi+f\phi_\xi-S\phi_\tau)-Sc\delta_2\left(S^2\phi_{\tau\tau}-S(f_\tau\phi_\xi+g_\tau\phi_\xi)-2S(g+f)\phi_{\tau\xi}+(g+f)^2\phi_{\xi\xi}+(f_\xi+g_\xi)(f+g)\phi_\xi\right)+\frac{N_t}{N_b}\theta_{\xi\xi}-Sc\Delta(1+\Lambda\theta)^m\phi\exp\left(-\frac{\Theta}{1+\Lambda\theta}\right)=0, \tag{12}$$

$$\chi_{\xi\xi}+\Upsilon(g\chi_\xi+\mathrm{f}\chi_\xi-\mathrm{S}\chi_\tau)-\beta((\chi+\Gamma)\phi_{\xi\xi}+\chi_\xi\phi_\xi)=0. \tag{13}$$

With boundary assumptions:

$$\left.\begin{array}{lllll}f_\xi(0,\tau)=\sin\tau, & f(0,\tau)=0, & g_\xi(0,\tau)=\gamma\sin\tau, & & g(0,\tau)=0,\\g_\xi(\infty,\tau)=0, & f_\xi(\infty,\tau)=0, & g_{\xi\xi}(\infty,\tau)=0, & f_{\xi\xi\xi}(\infty,\tau)=0, & \chi(0,\tau)=1,\\\theta(0,\tau)=1, & \phi(0,\tau)=1, & \chi(\infty,\tau)=0, & \theta(\infty,\tau)=0 & \phi(\infty,\tau)=0.\end{array}\right\} \tag{14}$$

The relevant involved parameters like Ψ (Deborah number), H (Magnetic parameter), ϖ (mixed convection), N (buoyancy ratio parameter), Π (bioconvected Rayleigh number), Pr (Prandtl number), Ξ (heat generation constant), $\mathrm{N_b}$ (Brownian motion), δ_1 (thermic relaxation constant), $\mathrm{N_t}$ (thermophoresis), S(angular frequency to stretching rate ratio), Sc (Schmidt number), δ_2 (solutal relaxation), Δ (reaction rate), Υ (bioconvected Lewis number), Λ (temperature difference), β (bioconvected Peclet number), Θ (activation energy), Γ (concentration difference constant for microorganisms) and γ (stretching ratio) are delineated as:

$$\left.\begin{array}{llll}S=\frac{\omega}{a}, & \varpi=\frac{\wp g(1-C_\infty)(T_w-T_\infty)}{a^2x}, & \mathrm{N}=\frac{(\rho_p-\rho_f)(C_w-C_\infty)}{\rho_f\wp(1-C_\infty)(T_w-T_\infty)}, & \mathrm{H}=\sqrt{\frac{\vartheta\mathbf{B}_0^2}{a\rho_{\tilde{f}}}},\quad \Xi=\frac{Q}{(\rho c)_f a},\\\Psi=\alpha_* a, & \Pi=\frac{\sigma_*(\rho_m-\rho_f)(n_w-n_\infty)}{\rho_f\wp(1-C_\infty)(T_w-T_\infty)}, & \delta_1=\delta_{\tilde{T}}a, & Sc=\frac{\nu}{D_B},\quad \delta_2=\delta_{\tilde{C}}a,\\\Upsilon=\frac{\nu}{D_m}, & \Delta=\frac{\mathrm{K}_r^{\ 2}}{a}, & \beta=\frac{\Re\Im}{D_m}, & \gamma=\frac{b}{a},\quad \mathrm{N_b}=\frac{\mho D_B(C_w-C_\infty)}{\nu},\quad \Lambda=\frac{(T_w-T_\infty)}{\tilde{T}_\infty},\\\mathrm{N_t}=\frac{\mho D_{\tilde{T}}(T_w-T_\infty)}{\nu T_\infty}, & \mathrm{Pr}=\frac{\mu c_p}{k_\infty}. & \Gamma=\frac{n_\infty}{n_w-n_\infty}. & \Theta=\frac{E_\odot}{\beta_\odot\tilde{T}_\infty}.\end{array}\right\} \tag{15}$$

The stimulating physical quantities like local Sherwood $\left(Sh_{\tilde{x}}\right)$, motile density $\left(Nn_{\tilde{x}}\right)$ and local Nusselt $\left(Nu_{\tilde{x}}\right)$ numbers are revealed as:

$$Sh_x=\frac{x\mathfrak{K}}{D_B\left(C_w-C_\infty\right)},\qquad Nn_x=\frac{x\varsigma}{D_m\left(n_w-n_\infty\right)},\qquad Nu_x=\frac{x\Diamond}{k\left(T_w-T_\infty\right)}, \tag{16}$$

Where mass, motile microorganisms and heat surface fluxes $\mathfrak{K},\varsigma,\Diamond$ are shown as:

$$\left.\begin{array}{lll}\mathfrak{K}=-D_B\left(\frac{\partial C}{\partial z}\right)_{z=0}, & \varsigma=-D_m\left(\frac{\partial n}{\partial z}\right)_{z=0}, & \Diamond=-k\left(\frac{\partial T}{\partial z}\right)_{z=0}.\end{array}\right\} \tag{17}$$

In view of dimensionless variables (8), we attained.

$$Sh_{\tilde{x}} = -\phi_{\xi}(0,\tau)\sqrt{Re_{\tilde{x}}}, \qquad Nn_{x^{\sim}} = -\chi_{\xi}(0,\tau)\sqrt{Re_{\tilde{x}}}, \\ Nu_{x^{\sim}} = -\theta_{\xi}(0,\tau)\sqrt{Re_{\tilde{x}}}. \tag{18}$$

3. Homotopy analysis method

Current physical model problem after utilization of (8) is transformed into highly nonlinear non-dimensional expressions (9–13) with transmuted boundary constraints (14) and almost it is hard to find exact solution of such complicated expressions. Homotopy analysis procedure (HAM) along with MATHEMATICA software is employed to attain analytic solution with amazing outcomes. The convergence analytic region and solution guesstimates can simply be determined and adjusted. This procedure does not demand any kind of constraints like large/small parameters and further not comprise discretization processes as in numerical techniques. This commanding analytic procedure was originally recommended by Liao [37] and afterward many researchers adopted this practice [38–40]. Initial estimates for current flow problems are:

$$\left.\begin{aligned} f_0(\xi,\tau) &= \sin\tau(1-\exp(-\xi)),\ \theta_0(\xi,\tau) = \exp(-\xi),\ \chi_0(\xi,\tau) = \exp(-\xi), \\ g_0(\xi,\tau) &= \gamma\sin\tau(1-\exp(-\xi)), \qquad \phi_0(\xi,\tau) = \exp(-\xi). \end{aligned}\right\} \tag{19}$$

The linear auxiliary operators for specified values of time are defined as:

$$L_f = \frac{\partial^3}{\partial\xi^3} - \frac{\partial}{\partial\xi}, \quad L_g = \frac{\partial^3}{\partial\xi^3} - \frac{\partial}{\partial\xi}, \quad L_\theta = \frac{\partial^2}{\partial\xi^2} - 1, \quad L_\phi = \frac{\partial^2}{\partial\xi^2} - 1, \quad L_\chi = \frac{\partial^2}{\partial\xi^2} - 1. \tag{20}$$

satisfying.

$$\left.\begin{aligned} L_f\left(\sum_{k=0}^{2} \mathcal{Z}_{k+1} e^{(k-1)\xi}\right) &= 0, \quad L_g\left(\sum_{j=3}^{5} \mathcal{Z}_{k+1} e^{(k-4)\xi}\right) = 0, \quad L_\theta\left(\sum_{j=6}^{7} \mathcal{Z}_{k+1} e^{(-1)^k \xi}\right) = 0, \\ L_\phi\left(\sum_{k=8}^{9} \mathcal{Z}_{k+1} e^{(-1)^k \xi}\right) &= 0, \qquad\qquad L_\chi\left(\sum_{k=10}^{11} \mathcal{Z}_{k+1} e^{(-1)^k \xi}\right) = 0, \end{aligned}\right\} \tag{21}$$

in which, $\mathcal{Z}_j (j = 1,2,.....,12)$ symbolizes arbitrary constants.

The analytic homotopic solution measured here mostly be dependent on auxiliary parameters $(\hbar_\phi, \hbar_\theta, \hbar_\chi, \hbar_f, \hbar_g)$, and by assigning precise values to these parameters will commendably regulate and adjust the convergence area. Fig. 2 is drafted to locate convergence region for all these variables and further the permitted values for desired convergence are shown in Table 1.

4. Solution verification

The simulation simulated in previous section are verified numerically in Table 2. The comparison of obtained data is ensured by comparing with work of Ariel [41] for limiting case. Clearly, a good agreement is assessed between both studies.

5. Analysis and discussion of results

5.1. Analysis of results

This section is organized to discuss the essential characteristics of diverse flow parameters on microorganisms concentration $\chi(\xi,\tau)$, nanoparticles concentration $\phi(\xi,\tau)$, flow fields $(f_\xi(\xi,\tau), g_\xi(\xi,\tau))$, and temperature $\theta(\xi,\tau)$ through diverse plots in detail. Furthermore, different numerical tables are organized to confer the effects of varied related variables on local Sherwood, motile density, and Nusselt numbers. The whole analysis is computed by assigning fixed selected values to involved dimensionless variables as: $S = 0.1$, $\Omega = 0.4$, $\Psi = 0.3$, $\mathrm{H} = 0.6$, $\varpi = 0.1$, $\mathrm{N} = 0.2$, $\Pi = 0.2$, $\mathrm{Pr} = 1.2$, $\Xi = 0.2$, $\mathrm{N_b} = 0.1$, $\delta_1 = 0.1$, $\mathrm{N_t} = 0.2$, $Sc = 0.4$, $\delta_2 = 0.1$, $\Delta = 0.3$, $\Upsilon = 0.7$, $\Lambda = 0.1$, $\beta = 0.7$, $\Theta = 0.2$, $\Gamma = 0.4$, $\gamma = 0.4$, $\mathrm{m} = 0.5$, and $\varepsilon = 0.1$. Moreover, the numerical values of auxiliary parameters for all curves are taken as $\hbar_g = \hbar_\theta = \hbar_\phi = \hbar_\chi = -0.8$. These values of variables stay common for entire analysis except alteration in specific tables and figures.

The graphical portrayal of magnetic and mixed convection variables (H, ϖ) on $f_\xi(\xi,\tau)$ is expressed in Fig. 3. This graph interprets that larger estimates of ϖ (mixed convection) associated with velocity augmentation, while upsurge in H (Magnetic parameter) leads to reduce velocity in this direction. In fact, higher values of mixed convection ϖ further dominates the buoyancy force consequences which indeed enhance velocity distribution. Moreover, augmentation in magnetic variable H produces resistance in movement of nanofluid which reduce velocity significantly. The buoyancy ratio variable and bioconvected Rayleigh number (N, Π) for velocity in $\tilde{x}-$ direction is conferred in Fig. 4, which displays that both these parameters deteriorate the velocity in this direction. The physical impact of stretching ratio and magnetic parameters (γ, H) on velocity component in $\tilde{y}-$ direction is displayed in Fig. 5. These curves indicate that magnetic parameter has similar decreasing tendency on velocity distribution in this direction as prescribed along $\tilde{x}-$ direction (Fig. 3), but velocity distribution remarkably improves for higher estimates of stretching ratio variable. Fig. 6 expresses the change in velocity along $\tilde{y}-$ direction for bioconvected Rayleigh number and buoyancy ratio variable (Π, N). These curves interpret that these parameters increase velocity in this direction. Fig. 6(a–f) are prepared to find physical consequences of Ψ (Deborah number), S (angular frequency to stretching rate ratio) and Ω (ratio among relaxation and retardation times) on velocity fields $(f_\xi(\xi,\tau), g_\xi(\xi,\tau))$ versus τ at a fixed distance $\xi = 0.25$ from oscillatory surface. Fig. 7a, b) demonstrate that both velocity components periodically decelerate for enhancement in Ω and reaches at minimum levels. Physically, relaxation time is boosted for higher Ω by which additional time is required for nanofluid particles to endure equilibrium situation from disturbed system and thus this declaration in velocities happen. Fig. 7c, d divulges that both velocity components periodically accelerate and achieve maximum level for greater Ψ. Since, this variable related with retardation time and so that nanofluid viscosity lessens for enhancement in Ψ, which generates this increasing trend in velocity curves. Fig. 7e, f are prepared to deliberate the periodic outcomes of S on velocity fields versus time. This variable significantly descents velocity amplitudes and furthermore a distinguishable phase shift results for larger estimations of this parameter.

The graphical depiction of related variables on dimensionless temperature fields are briefly explained in Figs. 8–10. Physical characteristics of thermal conductivity and Brownian motion variables $(\varepsilon, \mathrm{N_b})$ are delineated in Fig. 8, which interprets that temperature curves show enhancing trends for augmentation in both variables. Since kinetic energy is enhanced by faster collision of nanofluid particles for higher $\mathrm{N_b}$ which definitely upsurge temperature distribution. Furthermore, heat transportation can be improved by choosing variable thermal conductivity. Fig. 9 shows the physical outcomes for thermophoresis and heat generation parameters $(\mathrm{N_t}, \Xi)$. Here, these variables effectively escalate the temperature distributions. In fact, higher $\mathrm{N_t}$ further improves the transmission of suspended nanoparticles to relatively cooler region

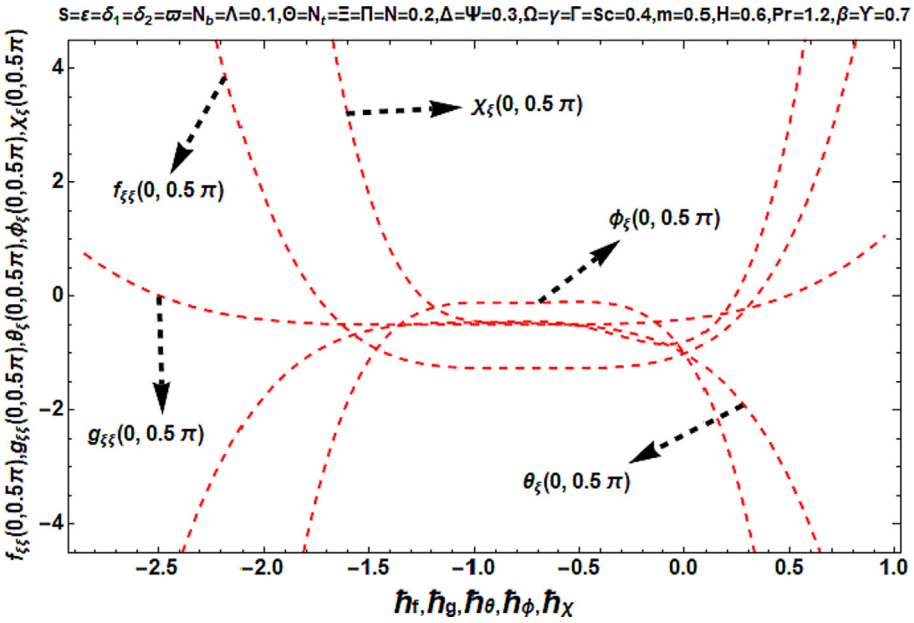

Fig. 2. h-curve profiles for velocities, motile microorganisms, concentration and temperature.

Table 1
Ranges for convergence control variables $(\hbar_\phi, \hbar_\theta, \hbar_\chi, \hbar_f, \hbar_g)$.

Estimated solutions	Convergent-control variables	Convergence region
$f(\xi,\tau)$	$\hbar_f$	$-1.2 \leqslant \hbar_f \leqslant -0.2$
$g(\xi,\tau)$	$\hbar_g$	$-1.9 \leqslant \hbar_g \leqslant -0.1$
$\theta(\xi,\tau)$	$\hbar_\theta$	$-1.5 \leqslant \hbar_\theta \leqslant -0.1$
$\phi(\xi,\tau)$	$\hbar_\phi$	$-1.1 \leqslant \hbar_\phi \leqslant -0.15$
$\chi(\xi,\tau)$	$\hbar_\chi$	$-1.15 \leqslant \hbar_\chi \leqslant -0.5$

by which temperature boost up. Moreover, additional heat is generated for enhancement in Ξ which ultimately intensify nanofluid temperature. Characteristics of Prandtl number and thermic relaxation constant (Pr, δ_1) has been portrayed in Fig. 10. It is seen that temperature remarkably drops for augmenting both variables. Physically, thermal diffusivity is diminished for larger Pr and subsequently nanofluid temperature descents. Moreover, thermic relaxation time increases for higher δ_1 by which heat conduction delays and temperature drops.

Figs. 11–13 are plotted to consider behavior of related variables for concentration sketches. Fig. 11 reports the graphical illustration of reaction rate and temperature difference variables (Δ, Λ). These curves show that the diverse expanding estimations of these variables exhibit deterioration in concentration and connected layer thickness. The profiles of nanoparticles concentration for varying activation energy and thermophoresis parameters $(\Theta, \mathrm{N_t})$ are revealed in Fig. 12, which articulates that concentration and connected layer thickness improves for augmenting both variables. Physically, reaction rate decreases for larger Θ consequently solute concentration upsurges. The enhancement in concentration profile is noted due to variation of thermophoresis parameter $\mathrm{N_t}$. The thermophoresis is famous phenomenon which is based on the migration of tiny particles from hot surface to the cooler regime due to temperature gradient. Due to migration of such particles, the improvement in the concentration profile has been observed. Fig. 13 is drawn to deliberate the physical consequences of solutal relaxation and Schmidt number (δ_2, Sc). The particular higher estimates of both variables correspond to lower the concentration and its related boundary thickness. Physically, higher δ_2 corresponds to increase solutal relaxation time by which nanoparticles concentration drops. Moreover, higher Sc induces lesser Brownian movement and nanoparticles concentration diminishes.

The physical characteristics of essential flow variables on microorganism's distribution has been observed in Figs. 14–15. To observe the significances of related variables like bioconvected Peclet and Lewis numbers (β, Y), Fig. 14 is organized. These curves show that enlarging both variables effectively decay this distribution. Since higher estimations of β and Y effectively reduce the microorganism' diffusivity by which motile density diminishes remarkably. The influence of microorganism's concentration difference and magnetic parameters (Γ, H) on $\chi(\xi,\tau)$ is graphically exhibited in Fig. 15. It is perceived that elevation in H improves the microorganism profile significantly, but proliferation in Γ show opposite trends.

To observe the physical behavior of relevant variables on concentration, temperature and microorganism distributions versus $\tau \in [0, 10\pi]$ at a distance $\xi = 0.15$ from accelerating surface, Figs. 16–18 are planned. The periodic influence of Ω is shown in

Table 2
Comparison of numerical computations when $S = \Omega = N = \Pi = \mathrm{H} = 0$.

γ	Ariel [41]				Present results	
	HPM		Exact			
	$-f''(0)$	$-g''(0)$	$-f''(0)$	$-g''(0)$	$-f''(0)$	$-g''(0)$
0.0	1.00000	0.00000	1.000000	0.000000	1.00000	0.00000
0.1	1.02025	0.06684	1.020259	0.066847	1.02026	0.06686
0.2	1.03949	0.14873	1.039495	0.148736	1.03950	0.14870

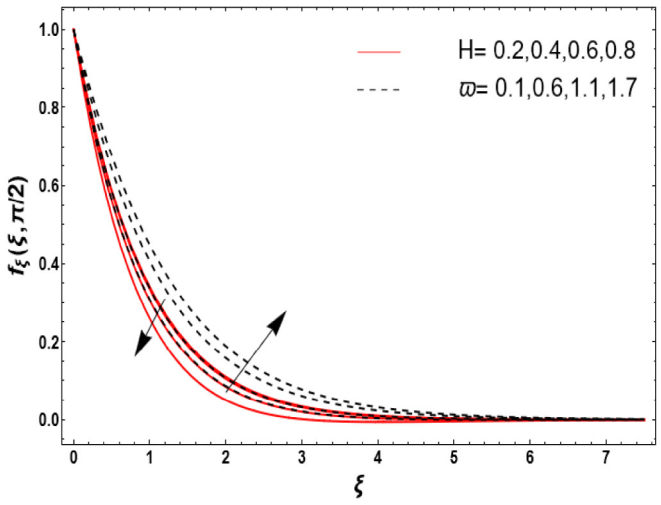

Fig. 3. Graphical influence of H & ϖ on f_ξ.

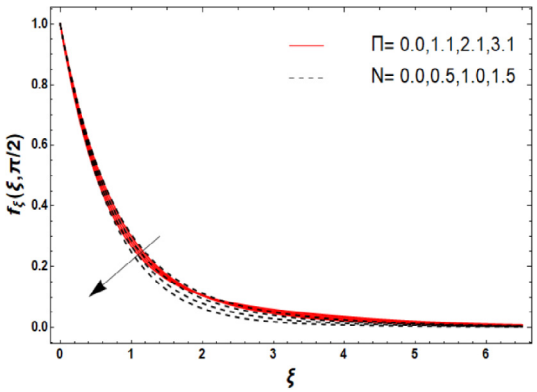

Fig. 4. Graphical influence of Π & N on f_ξ.

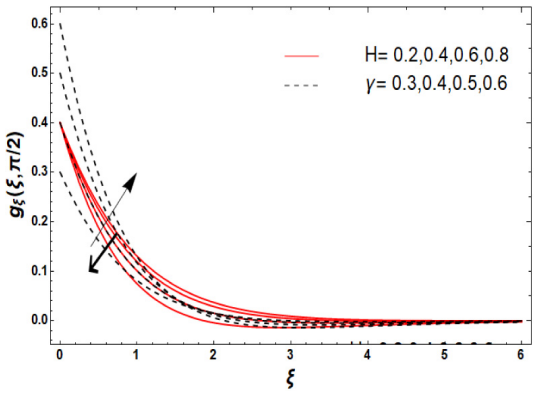

Fig. 5. Graphical influence of H & γ on g_ξ.

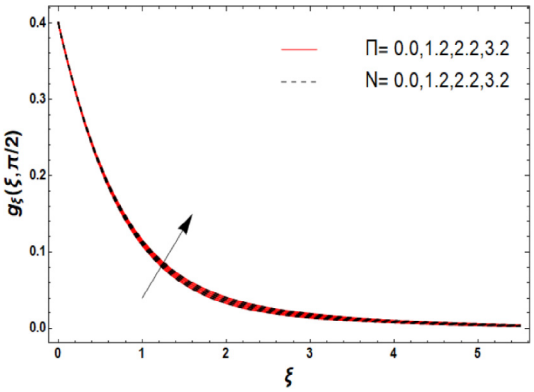

Fig. 6. Graphical influence of Π & N on g_ξ.

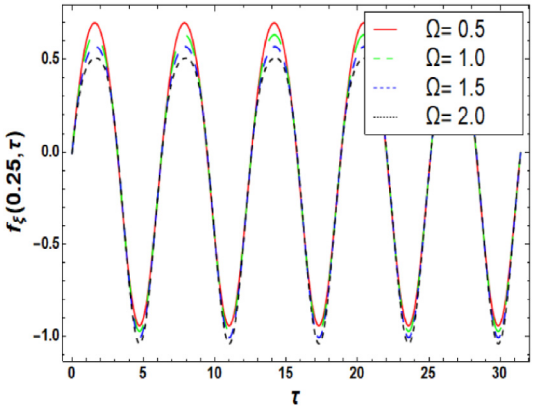

Fig. 7a. Graphical impact with time on f_ξ for Ω.

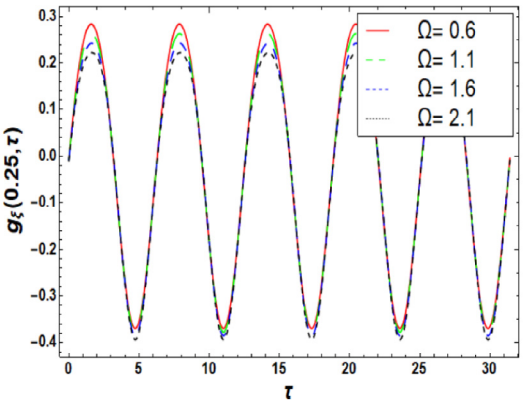

Fig. 7b. Graphical impact with time on g_ξ for Ω.

Fig. 16a–c, which indicates that all these distributions periodically accelerate and reaches at maximum level Fig. 17a–c are sketched to find influence of varying higher Ψ. It is seen from the curves that these distributions decrease periodically and attains minimum levels. Fig. 18a, b are prepared to find the graphical impact of δ_1 and δ_2 on temperature and concentration fields versus time, respectively. Here, amplitude of temperature distribution rises for improvent in δ_1, while same escalating trends in concentration distribution occurs for escalation in δ_2.

Tables 3–5 are organized to find the significances of diverse relevant variables on local Nusselt, Sherwood and motile density numbers, correspondingly. The physical influence of $\Omega, \Psi, \mathrm{Pr}, \delta_1, \varepsilon$ and Ξ on local Nusselt number is expressed in Table 3. Here, these tabular values indicate that heat transfer rate boosts for enlarging Ψ, Pr and δ_1, while other remaining variables show diminishing behavior. Table 4 interprets that mass transfer rate is intensified by augmenting the significant variables like Ω, Δ and Λ, but

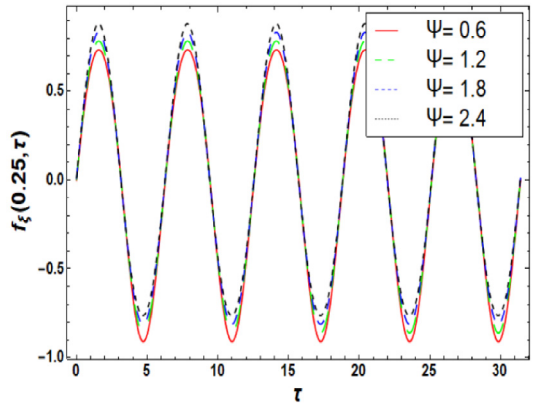

Fig. 7c. Graphical impact with time on f_ξ for Ψ.

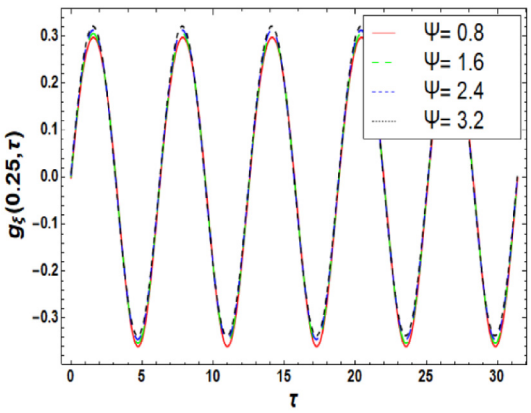

Fig. 7d. Graphical impact with time on g_ξ for Ψ.

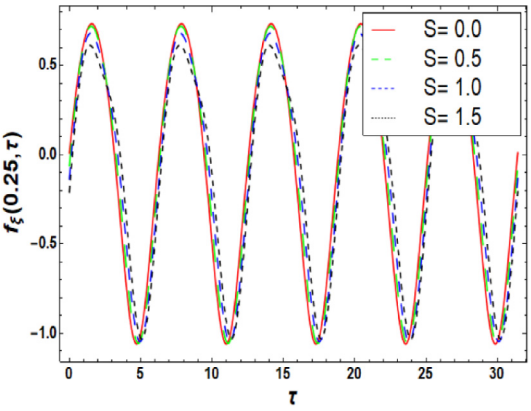

Fig. 7e. Graphical impact with time on f_ξ for *S*.

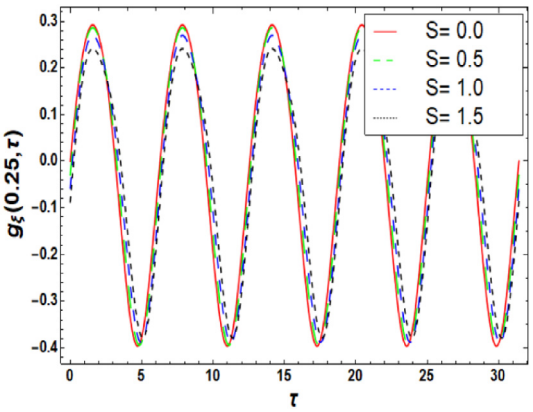

Fig. 7f. Graphical impact with time on g_ξ for *S*.

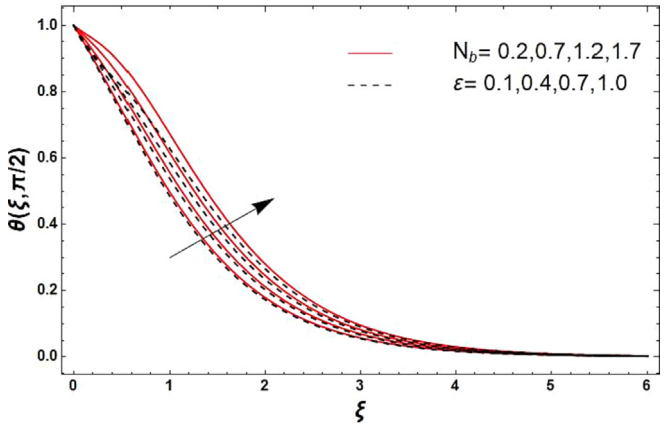

Fig. 8. Graphical influence of N_b & ε on θ.

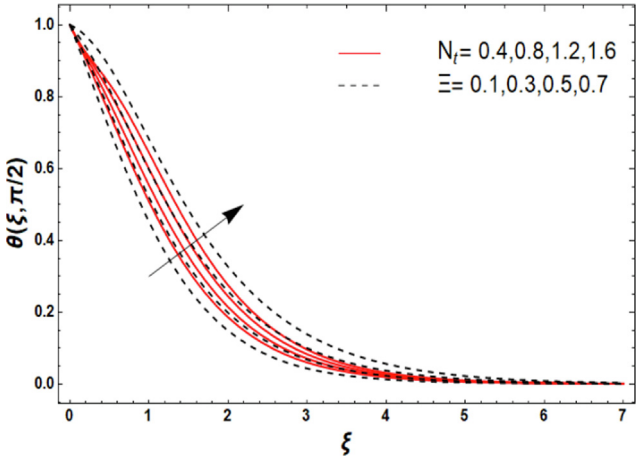

Fig. 9. Graphical influence of N_t & Ξ on.

enhancing values of Ψ, δ_2 and Θ lowers down the mass transformation rate significantly. Table 5 portrays the numerical outcomes for $\Omega, \Psi, \Upsilon, \beta, \Gamma$ and H on motile density number by keeping other variables fixed. This numerical data divulges that escalating Ω and H significantly reduce motile density number, while contrary outcomes are obtained for higher Ψ, Υ, β and Γ.

5.2. Discussion of results

The results for velocity profile as a function of time against variation of different parameters show oscillatory behavior. The oscillation in the velocity is observed without any phase shift except the variation of angular frequency to stretching rate ratio parameter. The pattern of magnitude of velocity remains uniform. No turbulent case is noted as the magnitude of oscillations in bidirectional moving surface has assumed to be small. The heat and mass transfer phenomenon enhanced for eclectically conductivity nanomaterials. An increasing change in the thermal profile due to variable viscosity parameter has been observed. Therefore, it

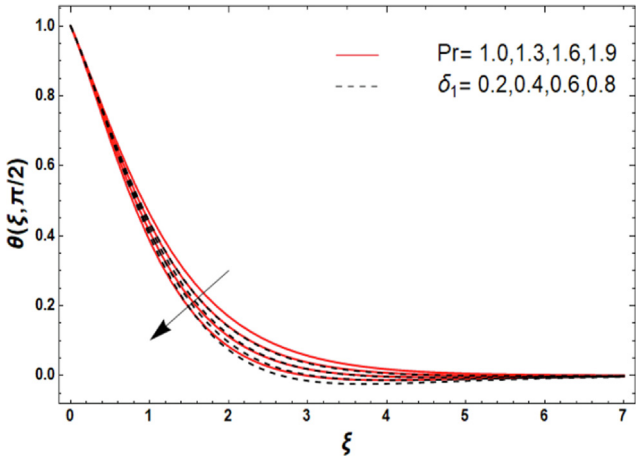

Fig. 10. Graphical influence of Pr & δ_1 on θ.

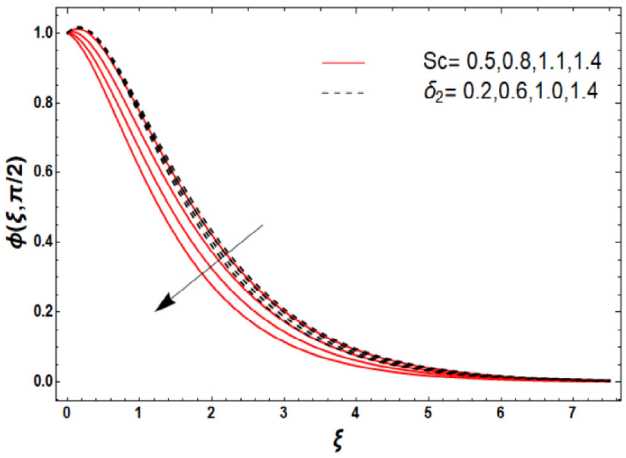

Fig. 13. Graphical influence of *Sc* & δ_2 on ϕ.

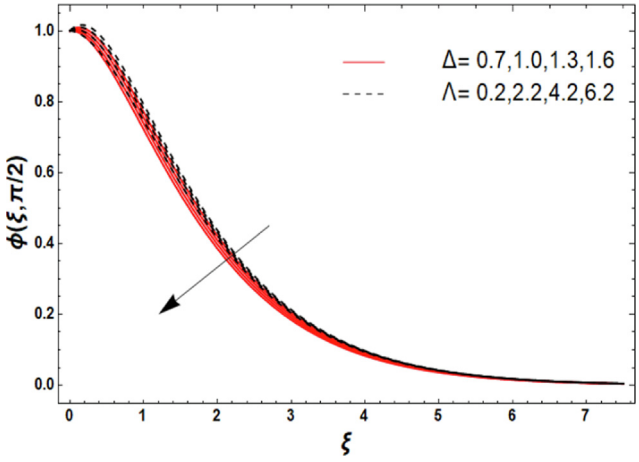

Fig. 11. Graphical influence of Δ & Λ on ϕ.

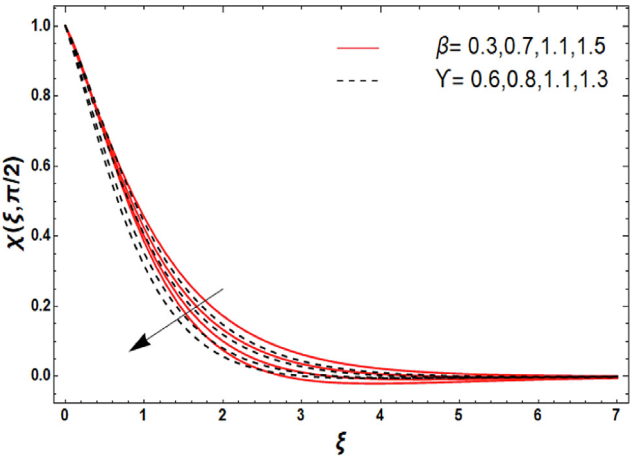

Fig. 14. Graphical influence of β & Y on χ.

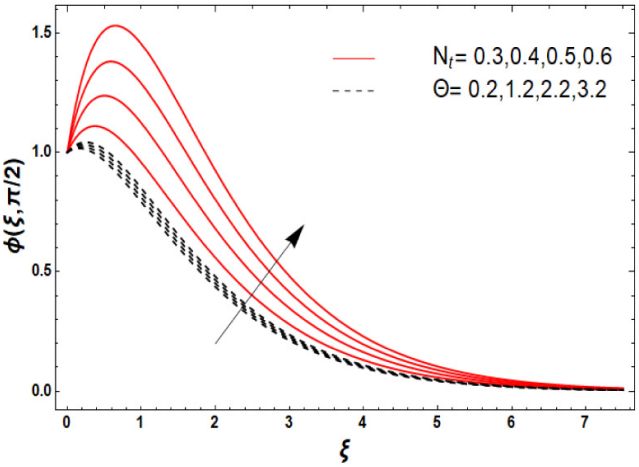

Fig. 12. Graphical influence of N_t & Θ on ϕ.

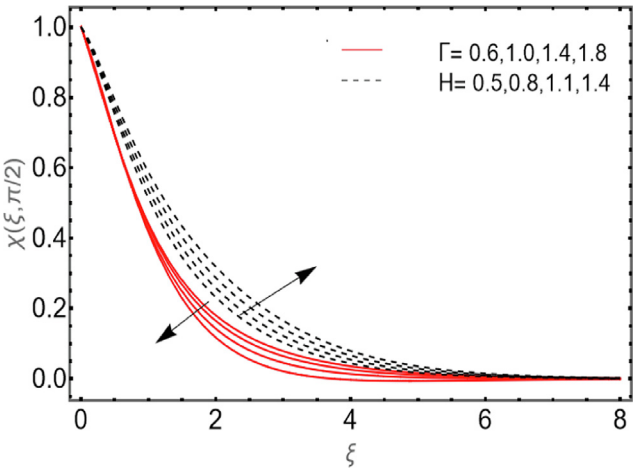

Fig. 15. Graphical influence of Γ & H on χ.

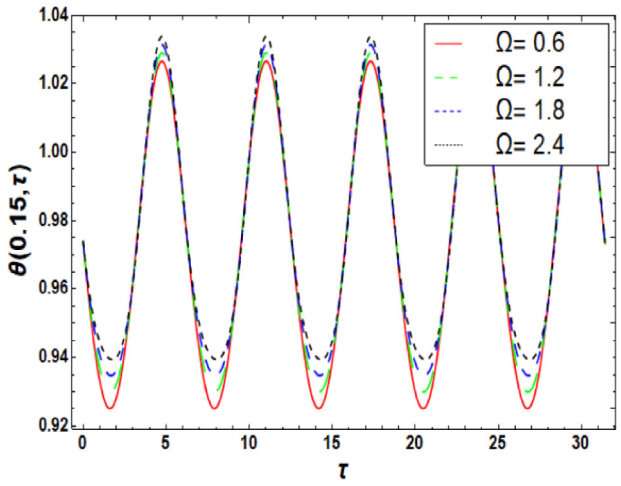

Fig. 16a. Graphical impact with time on θ for Ω.

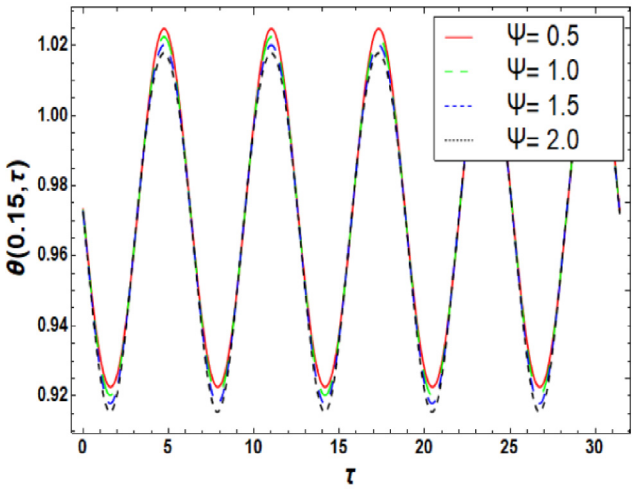

Fig. 17a. Graphical impact with time on θ for Ψ.

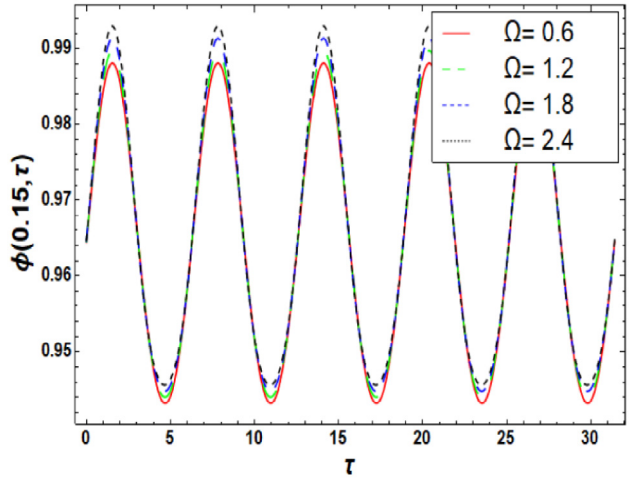

Fig. 16b. Graphical impact with time on ϕ for Ω.

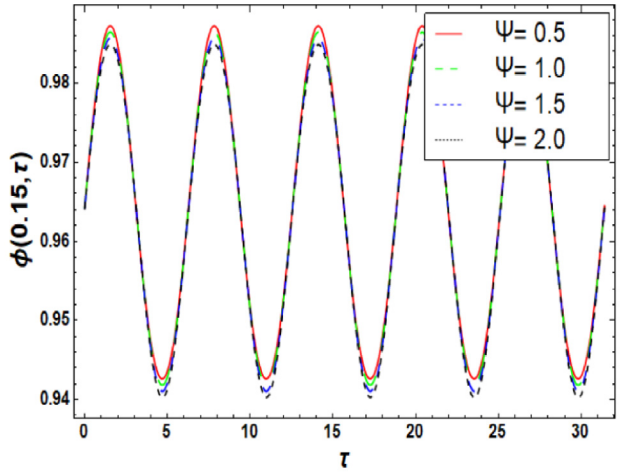

Fig. 17b. Graphical impact with time on ϕ for Ψ.

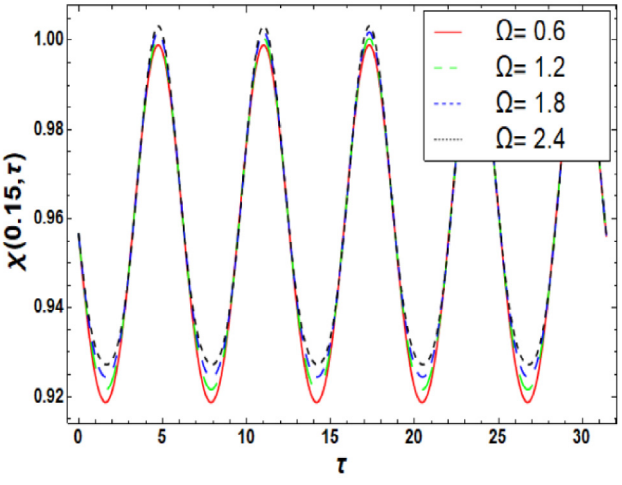

Fig. 16c. Graphical impact with time on χ for Ω.

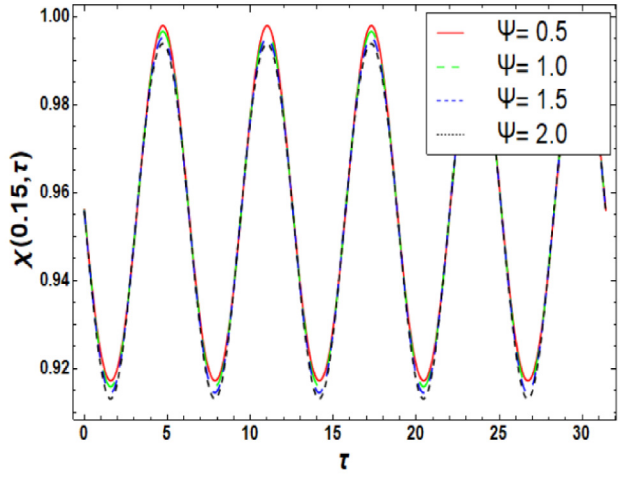

Fig. 17c. Graphical impact with time on χ for Ψ.

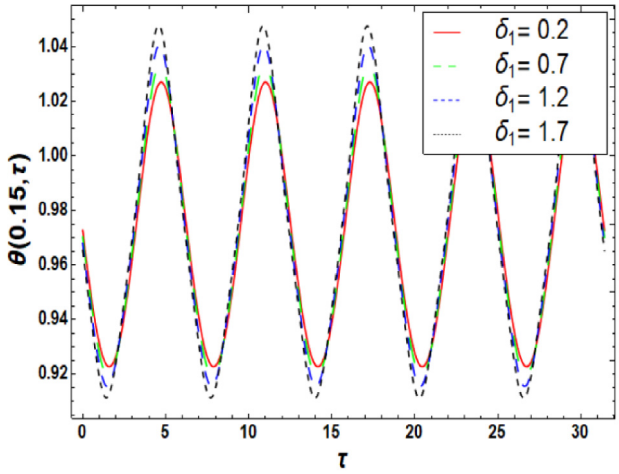

Fig. 18a. Graphical impact with time on θ for δ_1.

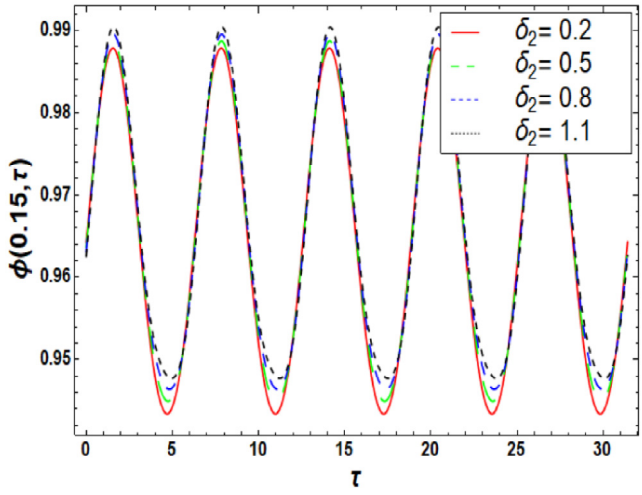

Fig. 18b. Graphical impact with time on ϕ for δ_2.

Table 3
Physical significances of $\Omega, \Psi, \mathrm{Pr}, \delta_1, \varepsilon$ and Ξ, at $\tau = \pi/2$ on $Nu_x(Re_x)^{-0.5}$.

Ω	Ψ	Pr	δ_1	ε	Ξ	$Nu_x(Re_x)^{-0.5}$
0.4	0.3	1.2	0.1	0.1	0.2	0.45889
0.5						0.44957
0.6						0.44077
0.4	0.5					0.47631
	0.7					0.49201
	0.9					0.50653
	0.3	0.7				0.36182
		1.1				0.43785
		1.5				0.52544
		1.2	0.2			0.47204
			0.3			0.48652
			0.4			0.50250
			0.1	0.3		0.40588
				0.5		0.37632
				0.7		0.36548
				0.1	0.4	0.23849
					0.6	−0.039821
					0.8	−0.39187

is suggested the consideration of variable viscosity of nanofluids is more effective to improve the thermal phenomenon. The thermal phenomenon can be controlled for specified values of Prandtl number.

Table 4
Physical significances of $\Omega, \Psi, \delta_2, \Delta, \Lambda$ and Θ, at $\tau = \pi/2$ on $Sh_x(Re_x)^{-0.5}$.

Ω	Ψ	δ_2	Δ	Λ	Θ	$Sh_x(Re_x)^{-0.5}$
0.4	0.3	0.1	0.3	0.1	0.2	0.10648
0.5						0.11056
0.6						0.11453
0.4	0.5					0.10144
	0.7					0.096577
	0.9					0.091970
	0.3	0.2				0.10399
		0.3				0.10147
		0.4				0.098894
		0.1	0.5			0.19625
			0.6			0.23921
			0.8			0.32148
			0.3	0.2		0.11194
				0.7		0.14088
				0.9		0.15321
				0.1	0.4	0.073754
					0.5	0.057127
					0.7	0.023333

Table 5
Physical significances of $\Omega, \Psi, \Upsilon, \beta, \Gamma$ and H, at $\tau = \pi/2$ on $Nn_x(Re_x)^{-0.5}$.

Ω	Ψ	Υ	β	Γ	H	$Nn_x(Re_x)^{-0.5}$
0.4	0.3	0.7	0.7	0.4	0.6	0.64226
0.5						0.63770
0.6						0.63343
0.4	0.5					0.65178
	0.7					0.66019
	0.9					0.66766
	0.3	0.5				0.55798
		1.0				0.76976
		1.5				0.97532
		0.7	0.6			0.62908
			1.1			0.69577
			1.6			0.76545
			0.7	0.5		0.64565
				0.9		0.65923
				1.3		0.67280
				0.4	0.5	0.64717
					0.9	0.62449
					1.6	0.48836

6. Conclusions

The thermal impact of Jeffrey nanofluid for bio-convective flow due to bidirectional accelerated frame has been studied theoratcially. Cattaneo-Christov diffusion theories are applied to consider mass and thermal transformation features. Thermal characteristics are further accomplished in presence of variable thermal conductivity and heat generation. Whole flow model is explored by considering activation energy and chemical reaction features. Major outcomes are:

- The decreasing impact of bioconvected Rayleigh number and buoyancy ratio parameter on velocity profile is noted.
- The temperature, microorganism and concentration profiles periodically accelerate for higher relaxation to retardation times parameter.
- Velocities periodically upsurge for enlarging Deborah number, but other distributions slow down periodically for this parameter.
- The consideration of variable thermal conductivity enhanced the temperature profile more exclusively.
- The nanoparticles concentration gets lessened for amplification in solutal relaxation and reaction rate variables, while conflicting consequences are achieved for activation energy.

- Microorganism distribution is deteriorated for enlarging bioconvective Peclet and Lewis numbers.
- The temperature amplitude increases for thermic relaxation parameter.

Declaration of Competing Interest

The authors declare that they have no known competing financial interests or personal relationships that could have appeared to influence the work reported in this paper.

Acknowledgments

The author extends their appreciation to the deputyship for Research & Innovation, Ministry of Education in Saudi Arabia for funding this research work through the project number (IFP-2020-101).

References

[1] Sudarsana Reddy P, Sreedevi P, Chamkha Ali J. MHD boundary layer flow, heat and mass transfer analysis over a rotating disk through porous medium saturated by Cu-water and Ag-water nanofluid with chemical reaction. Powder Technol 2017;307:46–55.
[2] Sreedevi P, Reddy PS, Sheremet M. A comparative study of Al_2O_3 and TiO_2 nanofluid flow over a wedge with non-linear thermal radiation. Int J Numer Meth Heat Fluid Flow 2020;30(3):1291–317.
[3] Reddy PS, Sreedevi P, Chamkha AJ. Heat and mass transfer analysis of nanofluid flow over swirling cylinder with Cattaneo-Christov heat flux. J Therm Anal Calorim 2022;147:3453–68.
[4] Sreedevi P, Reddy PS. Williamson hybrid nanofluid flow over swirling cylinder with Cattaneo-Christov heat flux and gyrotactic microorganism. Waves Random Complex Media 2021. doi: https://doi.org/10.1080/17455030.2021.1968537.
[5] Abdelsalam SI, Mekheimer KS, Zaher AZ. Dynamism of a hybrid Casson nanofluid with laser radiation and chemical reaction through sinusoidal channels. Waves Random Complex Media 2022. doi: https://doi.org/10.1080/17455030.2022.2058714.
[6] Alsharif AM, Abdellateef AI, Elmaboud YA, Abdelsalam SI. Performance enhancement of a DC-operated micropump with electroosmosis in a hybrid nanofluid: fractional Cattaneo heat flux problem. Appl Math Mech-Engl Ed 2022;43:931–44.
[7] Thirupathi Thumma, Mishra SR, Abbas MA, Bhatti MM, Abdelsalam SI. Three-dimensional nanofluid stirring with non-uniform heat source/sink through an elongated sheet. Appl Math Comput 2022;421:126927.
[8] Bhatti MM, Bég OA, Abdelsalam SI. Computational framework of magnetized MgO-Ni/water-based stagnation nanoflow past an elastic stretching surface: application in solar energy coatings. Nanomaterials (Basel) 2022;12(7):1049.
[9] Mekheimer KS, Abo-Elkhair RE, Abdelsalam SI, Ali KK, Moawad AMA. Biomedical simulations of nanoparticles drug delivery to blood hemodynamics in diseased organs: synovitis problem. Int Commun Heat Mass Transf 2022;130:105756.
[10] Liu G, Shengbin W, Shahsavari D, Karami B, Tounsi A. Dynamics of imperfect inhomogeneous nanoplate with exponentially-varying properties resting on viscoelastic foundation. Eur J Mech A Solids 2022;95:104649.
[11] Van Vinh P, Tounsi A, Belarbi MO. On the nonlocal free vibration analysis of functionally graded porous doubly curved shallow nanoshells with variable nonlocal parameters. Eng Comput 2022. doi: https://doi.org/10.1007/s00366-022-01687-6.
[12] Vinh P, Tounsi A. Free vibration analysis of functionally graded doubly curved nanoshells using nonlocal first-order shear deformation theory with variable nonlocal parameters. Thin-Walled Struct 2022;174:109084.
[13] Bouafia H, Chikh A, Bousahla AA, Bourada F, Heireche H, Tounsi A, Benrahou KH, Tounsi A, Al-Zahrani MM, Hussain M. Natural frequencies of FGM nanoplates embedded in an elastic medium. Adv Nano Res 2021;11(3):239–49.
[14] Heidari F, Taheri K, Sheybani M, Janghorban M, Tounsi A. On the mechanics of nanocomposites reinforced by wavy/defected/aggregated nanotubes. Steel Compos Struct 2021;38(5):533–45.
[15] Song Y-Q, Obideyi BD, Shah NA, Animasaun IL, Mahrous YM, Chung JD. Significance of haphazard motion and thermal migration of alumina and copper nanoparticles across the dynamics of water and ethylene glycol on a convectively heated surface. Case Stud Therm Eng 2021;26:101050.
[16] Oke AS, Animasaun IL, Mutuku WN, Kimathi M, Shah NA, Saleem S. Significance of Coriolis force, volume fraction, and heat source/sink on the dynamics of water conveying 47 nm alumina nanoparticles over a uniform surface. Chin J Phys 2021;71:716–27.
[17] Rajakarunakaran SA, Lourdu AR, Muthusamy S, Panchal H, Alrubaie AJ, Jaber MM, et al. Prediction of strength and analysis in self-compacting concrete using machine learning based regression techniques. Adv Eng Softw 2022;173:. doi: https://doi.org/10.1016/j.advengsoft.2022.103267. ISSN 0965-9978103267.
[18] Liu X, Adibi M, Shahgholi M, Iskander Tlili S, Sajadi M, Ali Abdollahi Z, et al. Phase change process in a porous carbon-paraffin matrix with different volume fractions of copper oxide nanoparticles: a molecular dynamics study. J Mol Liquids 2022;366:. doi: https://doi.org/10.1016/j.molliq.2022.120296. ISSN 0167-7322120296.
[19] Shuai Li S, Sajadi M, Khalid Abdulkhaliq M, Alharbi M-S, Tlili I. The molecular dynamics study of vacancy defect influence on carbon nanotube performance as drug delivery system. Eng Anal Bound Elem 2022;143:109–23. doi: https://doi.org/10.1016/j.enganabound.2022.06.006. ISSN 0955-7997.
[20] Huhemandula, Bai J, Kadir DH, Fagiry MA, Tlili I. Numerical analysis and two-phase modeling of water graphene oxide nanofluid flow in the riser condensing tubes of the solar collector heat exchanger. Sustain Energy Technol Assess 2022;53(Part A):. doi: https://doi.org/10.1016/j.seta.2022.102408. ISSN 2213-1388102408.
[21] Khan SU, Shehzad SA. Analysis for time-dependent flow of Carreau nanofluid over an accelerating surface with gyrotactic microorganisms: model for extrusion systems. Adv Mech Eng 2019;11(12):1–11.
[22] Waqas M, AdilSadiq M, Bahaidarah HMS. Gyrotactic bioconvection stratified flow of magnetized micropolar nanoliquid configured by stretchable radiating surface with Joule heating and viscous dissipation. Int Commun Heat Mass Transfer 2022;138:106229.
[23] Azam M, Xu T, Mabood F, Khan M. Non-linear radiative bioconvection flow of cross nano-material with gyrotatic microorganisms and activation energy. Int Commun Heat Mass Transfer 2021;127:105530.
[24] Hussain S, Raizah Z, Aly AM. Thermal radiation impact on bioconvection flow of nano-enhanced phase change materials and oxytactic microorganisms inside a vertical wavy porous cavity. Int Commun Heat Mass Transfer 2022;139:106454.
[25] Habib U, Abdal S, Siddique I, Ali R. A comparative study on micropolar, Williamson, Maxwell nanofluids flow due to a stretching surface in the presence of bioconvection, double diffusion and activation energy. Int Commun Heat Mass Transfer 2021;127:105551.
[26] Al-Khaled Y-M, Khan N, Khan MI, Khan SU, Hashmi MS, Iqbal MA, Tlili I. Study of Buongiorno's nanofluid model for flow due to stretching disks in presence of gyrotactic microorganisms. Ain Shams Eng. J. 2021;12(4):3975–85.
[27] Xia W-F, Haq F, Saleem M, Khan MI, Khan SU, Chu Y-M. Irreversibility analysis in natural bio-convective flow of Eyring-Powell nanofluid subject to activation energy and gyrotactic microorganisms. Ain Shams Eng. J. 2021;12(4):4063–74.
[28] Habib D, Salamat N, Abdal S, Siddique I, Ang MC, Ahmadian A. On the role of bioconvection and activation energy for time dependent nanofluid slip transpiration due to extending domain in the presence of electric and magnetic fields. Ain Shams Eng J 2022;13(1):101519.
[29] Elbashbeshy EMA, Asker HG, Nagy B. The effects of heat generation absorption on boundary layer flow of a nanofluid containing gyrotactic microorganisms over an inclined stretching cylinder. Ain Shams Eng J 2022;13(5):101690.
[30] Makinde OD, Animasaun IL. Bioconvection in MHD nanofluid flow with nonlinear thermal radiation and quartic autocatalysis chemical reaction past an upper surface of a paraboloid of revolution. Int J Therm Sci 2016;109:159–71.
[31] Animasaun IL, Shah NA, Wakif A, Mahanthesh B, Sivaraj R, Koriko OK. Ratio of momentum diffusivity to thermal diffusivity: introduction, meta-analysis, and scrutinization. New York: Chapman and Hall/CRC; 2022.
[32] Shahzad F, Jamshed W, Nisar KS, Khashan MM, Abdel-Aty A-H. Computational analysis of Ohmic and viscous dissipation effects on MHD heat transfer flow of Cu-PVA Jeffrey nanofluid through a stretchable surface. Case Stud Therm Eng 2021;26:101148.
[33] Rafiq M, Sajid M, Alhazmi SE, Ijaz Khan M, El-Zahar ER. MHD electroosmotic peristaltic flow of Jeffrey nanofluid with slip conditions and chemical reaction. Alex Eng J 2022;61(12):9977–92.
[34] Haq F, Khan MI, Khan SU, Abualnaja KM, El-Shorbagy MA. Physical aspects of magnetized Jeffrey nanomaterial flow with irreversibility analysis. Chin Phys B 2022;31:084703.
[35] Ahmad I, Aziz S, Ali N, Khan SU. Radiative unsteady hydromagnetic 3D flow model for Jeffrey nanofluid configured by an accelerated surface with chemical reaction. Heat Transfer Asian Res 2021;50(1):942–66.
[36] Aziz S, Ahmad I, Ali N, Khan SU. Unsteady 3D mixed convection flow of chemically reactive Oldroyd-B nanofluid configured by periodically accelerated surface. Heat Transfer Asian Res 2021;50(5):4462–80.
[37] Liao SJ. Advance in the homotopy analysis method. 5 Toh Tuck Link. Singapore: World Scientific Publishing; 2014.
[38] Liao SJ. Beyond perturbation: introduction to homotopy analysis method. CRC Press, Boca Raton: Chapman & Hall; 2003.
[39] S.J. Liao, Homotopy Analysis Method in Nonlinear Differential Equations, 2012, ISBN: 978-3-642-25131-3.
[40] Turkyilmazoglu M. Some issues on HPM and HAM methods: a convergence scheme. Math Comput Model 2011;53:1929–36.
[41] Ariel PD. The three-dimensional flow past a stretching sheet and the homotopy perturbation method. Comput Math Appl 2007;54:920–5.